FERMILAB-PUB-15-098-APC
ACCEPTED

nuSTORM and a Path to a Muon Collider

David Adey,[1] Ryan Bayes,[3] Alan D. Bross,[1] and Pavel Snopok[2]

[1] Accelerator Physics Center, Fermi National Accelerator Laboratory, Batavia, USA, 60515
[2] Physics Department, Illinois Institute of Technology, Chicago, USA, 60616
[3] School of Physics and Astronomy/University of Glasgow, Glasgow, UK, G12 8QQ

Xxxx. Xxx. Xxx. Xxx. YYYY. AA:1–32

This article's doi:
10.1146/((please add article doi))

Keywords

sterile neutrinos, neutrino cross sections, ionization cooling, muon collider

Abstract

This article reviews the current status of the nuSTORM facility and shows how it can be utilized to perform a next step on the path towards the realization of a $\mu^+\mu^-$ collider. The article includes the physics motivation behind nuSTORM, a detailed description of the facility and the neutrino beams it can produce and a summary of the short-baseline neutrino oscillation physics program that can be carried out at the facility. The basic idea for nuSTORM (the production of neutrino beams from the decay of muons in a racetrack-like decay ring) was discussed in the literature over 30 years ago in the context of searching for non-interacting ("sterile") neutrinos. However, it was only in the past five years that the concept was fully developed, motivated again in large part, by the facility's unmatched reach in addressing the evolving data on oscillations involving sterile neutrinos. Finally, the article reviews the basics of the $\mu^+\mu^-$ collider concept and elucidates on how nu STORM provides a platform to test advanced concepts for 6D muon ionization cooling.

Contents

1. Overview

The nuSTORM facility (1–3) is the simplest implementation of the Neutrino Factory concept (4) and is based almost entirely on well-demonstrated accelerator technology, thus making its implementation technically feasible at this writing. At the heart of the facility is a racetrack-like muon storage ring that can deliver beams of $\overset{(-)}{\nu}_e$ and $\overset{(-)}{\nu}_\mu$ from the decay of stored $\mu^\pm$ beams. At nuSTORM, searches can be carried out to look for the existence of sterile neutrinos, while simultaneously, a physics program can operate that serves future long- and short-baseline neutrino-oscillation programs by providing definitive (percent-level precision) measurements of $\overset{(-)}{\nu}_e N$ and $\overset{(-)}{\nu}_\mu N$ scattering cross sections over a wide (0.5 to $\simeq$ 4 GeV) neutrino energy range. The facility also provides a platform to develop and test concepts for 6D muon cooling and thus facilitates the R&D path for a muon collider.

NEUTRINO BEAMS

It has been over 50 years since Simon van der Meer invented the magnetic horn in order to improve the performance of neutrino beam production. The nuSTORM facility provides a technically-ready opportunity to finally move beyond this paradigm.

The front end of nuSTORM is essentially identical to a conventional neutrino beam where protons (80-120 GeV) are used to produce pions off a conventional solid target and the pions are then focused with a magnetic horn (5). From this point on, nuSTORM departs significantly from a conventional neutrino beam. After the horn, quadrupole magnets are

Figure 1

Schematic layout of the nuSTORM facility

used to transport the pions to a chicane (double bend for sign selection) and then either a π^- or π^+ beam is transported to, and injected into, the decay ring. The pions that decay in the first straight of the ring can yield muons that are captured in the ring. [Note: The pion decays also produce a very powerful ν_μ beam, see section 5.1]. The circulating muons then subsequently decay into electrons and neutrinos. The nuSTORM facility uses a storage ring design that was optimized for a 3.8 GeV/c muon central momentum. This momentum was selected to maximize the physics reach for both ν oscillation and ν cross-section physics. See **Figure 1** for a schematic of the facility. The physics potential of nuSTORM, as in the case of the Neutrino Factory (6), comes from the fact that muon decay yields a neutrino beam of precisely known flavor content and energy (the muon energy being defined by the ring lattice). If the circulating muon flux in the ring is measured accurately (with beam-current transformers, for example), then the neutrino beam flux can be determined to high precision ($\lesssim 1\%$). This level of precision can be obtained without the need for any input or assumptions regarding particle production rates, proton targeting stability, target structural stability or horn pulse-to-pulse uniformity, the understanding of which is of tremendous importance for a conventional neutrino beam.

2. nuSTORM's physics program: Three themes

The physics program for the nuSTORM facility encompasses three central themes.

1. The neutrino beams produced at the nuSTORM facility will enable short-baseline (SBL) oscillation searches for light-sterile neutrinos with unprecedented sensitivity over a wide parameter space and, if sterile neutrinos are discovered, offers the opportunity to carry out an extremely comprehensive study of their properties.
2. These same beams may be exploited to make detailed studies of neutrino-nucleus scattering over the neutrino-energy range of interest to present and future long-baseline (LBL) neutrino oscillation experiments such as T2HK (7), LBNE (8) and LBNO (9).
3. The storage ring itself, and the muon beam it contains, can be used to carry out a R&D program that can facilitate the implementation of the next step in the incremental development of muon accelerators for particle physics.

These three individually-compelling themes provide the scientific and technological case for nuSTORM.

2.1. Sterile neutrinos

Sterile neutrinos are a generic ingredient of many extensions of the Standard Model and, even in models that do not contain them, can usually be easily added. One important class of sterile neutrino theories are models explaining the smallness of neutrino masses by means of a seesaw mechanism. In its simplest form, the seesaw mechanism requires at least two heavy ($\sim 10^{14}$ GeV) sterile neutrinos that would have very small mixings ($\sim 10^{-12}$) with the active neutrinos. However, in slightly non-minimal models, at least one sterile neutrino can have a much smaller mass and a much larger mixing angle. Examples of this type of model include the "inverse seesaw" (10; 11) and the split seesaw (12) scenarios. For a detailed review of models with sterile neutrinos and their associated phenomenology, see (13).

2.1.1. Experimental status for light-sterile neutrinos.

Much of the current interest in light-sterile neutrinos is motivated by experimental data. Results from the LSND (14) and MiniBooNE (15) experiments, the GALLEX and SAGE solar-neutrino experiments (16–20) and a re-analysis (13; 21–23) of short-baseline ($L \leq 100$ m) reactor experiments can be described by a 3+1 model with 3 active neutrinos and 1 sterile neutrino with a mass of $\simeq 1$ eV and small mixing. The appearance signals ($\nu_\mu \rightarrow \nu_e$ and $\bar{\nu}_\mu \rightarrow \bar{\nu}_e$) observed by LSND and MiniBooNE imply the existence of a corresponding disappearance signal via the following inequality (24):

$$\langle P_{\nu_\mu \rightarrow \nu_e} \rangle \leq 4 \left(1 - \langle P_{\nu_\mu \rightarrow \nu_\mu} \rangle\right) \left(1 - \langle P_{\nu_e \rightarrow \nu_e} \rangle\right) \tag{1}$$

where $\langle P_{\nu_\mu \rightarrow \nu_e} \rangle, \langle P_{\nu_\mu \rightarrow \nu_\mu} \rangle$ and $\langle P_{\nu_e \rightarrow \nu_e} \rangle$ are the energy-averaged oscillation probabilities for $\nu_\mu \rightarrow \nu_e$ appearance and $\nu_\mu \rightarrow \nu_\mu, \nu_e \rightarrow \nu_e$ disappearance, respectively. An analogous expression is valid for anti-neutrinos. This disappearance signal is observed in GALLEX and SAGE (ν_e) and in the short-baseline reactor experiments ($\bar{\nu}_e$). In spite of the interesting results from the experiments described above, the existence of light-sterile neutrinos is *far* from established. A number of other short baseline experiments did not observe an appearance signal (E776, KARMEN, NOMAD, ICARUS) (25–28) and strong constraints on a disappearance signal have been produced by numerous other experiments (data from long and short-baseline experiments, solar and atmospheric neutrino data, etc.) (17; 19; 29–57). These data place strong constraints on the available sterile neutrino parameter space. The compatibility of the signals from the LSND, MiniBooNE, reactor and gallium experiments with null results from the large number of other experiments has been assessed in global fits (13; 58–65). The results from one of these studies (65) are shown in **Figure 2**. The parameter region favored by the LSND, MiniBooNE, reactor and gallium experiments is incompatible, at the 99% confidence level, with exclusion limits from all other experiments. It is difficult to resolve this tension, even in models with more than one sterile neutrino. Recent results from DAYA BAY, MINOS+ and T2K (66–68) have put additional constraints on the allowed parameter space, but do not significantly alter the conclusions from Figure 2. It is important to note that in spite of the incompatibility between the appearance and disappearance data sets used in the global fit, taken individually, the different data sets are self-consistent. For example, $\overset{(-)}{\nu}_\mu \rightarrow \overset{(-)}{\nu}_e$ transitions with parameters suitable for explaining LSND and MiniBooNE are not directly ruled out by other experiments obtaining null results measuring the same oscillation channels (65).

Finally, cosmological observations constrain the effective number, N_{eff}, of neutrinos and the sum of neutrino masses, putting tight constraints on the allowed parameter space for

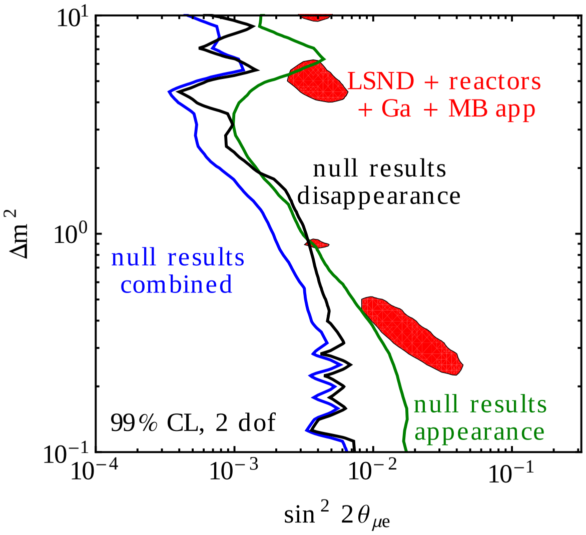

Figure 2

Results of a global fit (from ref. (65)) to data in a 3+1 sterile-neutrino model . The solid red areas indicate the regions preferred by the experiments reporting a signal (LSND, MiniBooNE, reactors and Gallium) versus the constraints imposed by disappearance null results (black), appearance null results (green) and all null results combined (blue).

light-sterile neutrinos. Recent Planck data (69) yields $N_{\rm eff} = 3.30^{+0.54}_{-0.51}$ when combined with polarization data from WMAP (70), high-multipole measurements from ACT (71) and SPT (72; 73) and data on baryon acoustic oscillations (BAO) (74–77). The same data impose a constraint on $\sum m_\nu \leq 0.230$ eV at the 95% C.L. However, cosmology only puts constraints on sterile neutrinos that are thermalized in the early Universe and models with sterile neutrinos, with so-called "hidden interactions" (78; 79), have been shown to reconcile the tension between cosmology and the experimental data indicating a light-sterile neutrino. A recent paper (80) has extended this argument, showing that this scenario would reduce $N_{\rm eff}$ down to 2.7.

We end our discussion on the experimental status of light-sterile neutrinos by stating that, given the current situation, it is impossible to draw firm conclusions regarding their existence. An experiment with superior sensitivity and precisely-controlled systematic uncertainties has great potential to clarify the situation by either finding a new type of neutrino oscillation or by producing a strong and robust constraint against any such oscillation.

2.2. Neutrino scattering physics: Systematics of LBL oscillation measurements

The recent measurement of a large value for the mixing angle, θ_{13}, has made observation of CP-violation in the lepton sector a fundamental (and now reachable) goal of the next generation of long baseline neutrino oscillation (LBL) experiments. Measurement of the CP-violating phase, δ_{CP}, can be accessed experimentally through two methods: a non-zero phase will lead to a difference between the $\nu_\mu \to \nu_e$ and $\bar{\nu}_\mu \to \bar{\nu}_e$ appearance probabilities as well as a variation in the relative amplitude of the second oscillation maximum with respect

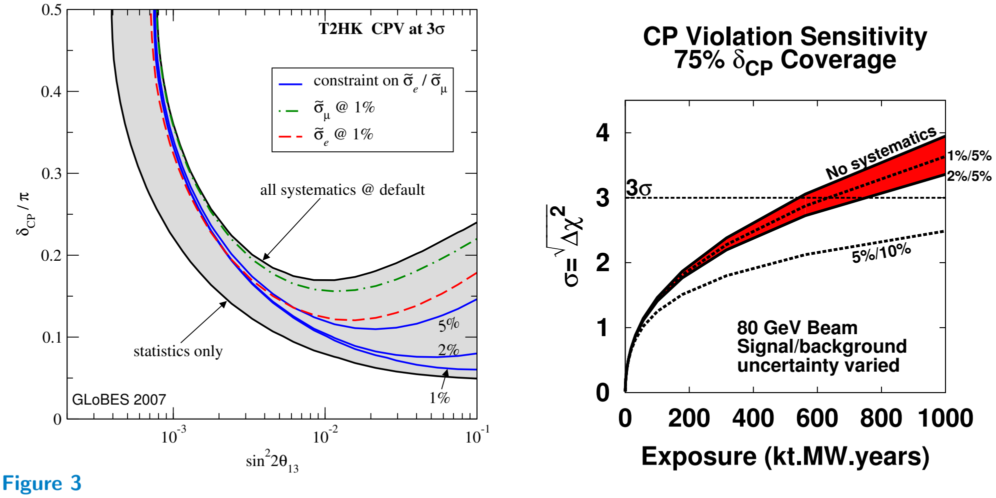

Figure 3

Left: CP violation sensitivity at 3σ for a certain choice of systematic errors and for statistical errors only (curves delimiting the shaded region). Also shown is the sensitivity if certain constraints on the product of cross sections times efficiencies $\tilde{\sigma}$ are available: 1% accuracies on $\tilde{\sigma}_\mu$ and $\tilde{\sigma}_e$ for neutrinos and antineutrinos, and 5%, 2%, 1% accuracies on the ratios $\tilde{\sigma}_\mu/\tilde{\sigma}_e$ for neutrinos and antineutrinos. Figure and caption adapted from Ref. (81). Right: Shown is the 75% CP violation reach of LBNE at 3σ confidence level as a function of the total exposure and its change under variations of the systematic error budget on signal normalization and background normalization respectively.

to the first oscillation maximum in $\nu_\mu \rightarrow \nu_e$ appearance measurements. Any experiment that is attempting to measure CP-violation using neutrino oscillations must be capable of measuring a small difference between small numbers of events and, in this context, it is imperative that all systematic errors be well controlled, either by external measurements, by measurements at near detectors or both. One of the largest systematic errors comes from poor knowledge of the neutrino ($\overset{(-)}{\nu}_e$ and $\overset{(-)}{\nu}_\mu$) interaction cross sections and an irreducible component of this uncertainty is knowledge of the neutrino flux. As we shall show, nuSTORM offers the possibility of reducing the neutrino flux uncertainties by upwards of a factor of ten.

In Ref. (81) a T2HK-like setup was studied where a total of more than 20 parameters, including total cross section uncertainties, were considered. One of the main results is shown in **Figure 3** (left), where the sensitivity to CP violation is shown both for statistical errors only, as well as for the full systematic error budget. It is obvious that a constraint on the ratio $\tilde{\sigma}_\mu/\tilde{\sigma}_e$ (where $\tilde{\sigma}_\mu$ and $\tilde{\sigma}_e$ are the product of cross section times detection efficiency for ν_μ and ν_e, respectively) is an efficient way to recover the desired statistical sensitivity. Another way to illustrate this problem is shown in Figure 3 (right). Here we show results from an LBNE study (24) where the capability to measure δ_{CP} at 3σ sensitivity over 75% of the parameter space is given as a function of exposure for various assumptions regarding the systematic error budget. In order to reach 75% coverage in a reasonable exposure time, systematic uncertainties at the 1% level are necessary. As can be seen in the figure, degradation of the systematic uncertainty to the 5% level corresponds to an exposure increase of roughly 200-300%, which occurs in a very non-linear fashion. In order to have the largest δ_{CP} coverage, the ratio $\tilde{\sigma}_\mu/\tilde{\sigma}_e$ needs to be understood at the few percent level.

3. The nuSTORM facility

The basic concept for the facility was presented in section 1. After the pions are transported to the decay ring, they are "stochastically" injected into the decay ring (82; 83) and pion decays within the first straight of this ring can yield a muon that will be stored in the ring. Muon decay produces ν beams of known flux and flavor via: $\mu^+ \rightarrow e^+ + \bar{\nu}_\mu + \nu_e$ or $\mu^- \rightarrow e^- + \nu_\mu + \bar{\nu}_e$. nuSTORM uses a storage ring with a central momentum of 3.8 GeV/c ($\pm$10%) in order to obtain a spectrum of neutrinos that peaks at $\simeq$ 2 GeV (see section 5.1). The pion beam line is optimized to capture and transport pions in a momentum band of 5 ± 1 GeV/c.

The stochastic injection scheme employed by nuSTORM, the feasibility of which was recently confirmed by Neuffer and Liu (84), avoids using a separate pion decay channel and fast kickers, thus only requires DC magnets. A schematic of this concept is given in **Figure 4**. The red box in this figure shows the components of the facility that comprise what has been termed the nuSTORM "pion beam line": pion collection downstream of the horn, transport to the ring, which involves a sign selection chicane, and then injection into the ring via the orbit combination section (OCS) (85). Pions that do not decay in the first straight are removed by an OCS mirror and transported to a beam absorber. Muons from forward decay, lying in the same momentum band of the initial pions, will also be extracted by the OCS mirror (see section 3.2).

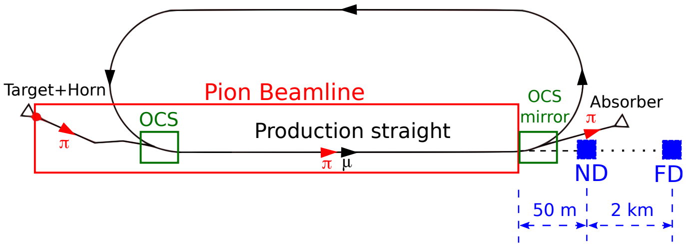

Figure 4

Schematic diagram of the nuSTORM facility. The position of the near and far (ND, FD) detector sites is also shown.

A complete engineering conceptual design for siting nuSTORM at Fermilab has been completed (86). **Figure 5** shows the nuSTORM facility components as they would be sited near the Fermilab. The design of the facility followed wherever possible (primary proton beam line, target, horn, etc.), NuMI (87) designs and consist of six components: the primary beam line, target station, transport line, muon decay ring, and near and far detector halls. Sited at Fermilab, nuSTORM operation extracts one "booster batch" ($\simeq 8 \times 10^{12}$ protons) at 120 GeV from the Main Injector (MI) and places this beam on target. This corresponds to 700 kW total beam power in the MI. The 1.6 μsec long booster batch's length is well matched to the 480 m circumference of the decay ring. Muons captured in the ring will have just returned to the OCS as pion injection stops. A layout concept for siting nuSTORM at CERN has also been developed (88; 89).

The primary proton beam line and target station (and its components, i.e., target and

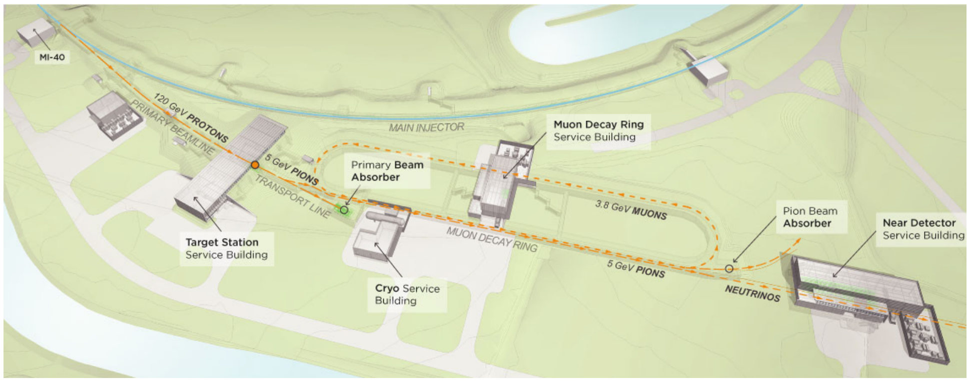

Figure 5

Engineering layout of the nuSTORM facility components showing the proton beam line from the Fermilab Main Injector, target station, pion transport line, decay ring and near detector hall.

horn) for nuSTORM can closely follow the NuMI designs. A horn optimization study (90) specifically for nuSTORM has been done, however. From the downstream end of the horn, the nuSTORM beam system is no longer similar to NuMI or any other conventional neutrino beam. From the downstream end of the horn, pion transport is continued with several radiation-hard (MgO insulated) quadrupoles. Although conventional from a magnetic field point of view, the first two to four quads need special and careful treatment in their design in order to maximize their lifetime in this high-radiation environment. Quadrupole magnets meeting the nuSTORM radiation-resistance criteria have been successfully built and operated, however (91). The pion beam is brought from the target station and transported through a chicane section to the injection OCS of the decay ring. **Figure 6** shows a G4Beamline (92) depiction of the pion transport line and the beginning of the decay ring FODO straight section. The decay ring straight-section FODO cells were designed to have betatron functions β_x, β_y (the Twiss parameters (93)) optimized for beam acceptance and neutrino beam production (small divergence relative to the muon opening angle $(1/\gamma)$ from $\pi \to \mu$ decay). Large betatron functions increase the beam size leading to aperture losses, while smaller betatron functions increase the divergence of the muon beam. In balancing these two criteria, FODO cells with $\beta_{\max}$=30.2 m, and $\beta_{\min}$=23.3 m were chosen for the 3.8 GeV/c muons. For the 5.0 GeV/c center momentum pions, this implies 38.5 m and 31.6 m for the pion's $\beta_{\max}$ and $\beta_{\min}$, respectively.

β function: Function related to the transverse size of a beam along its trajectory

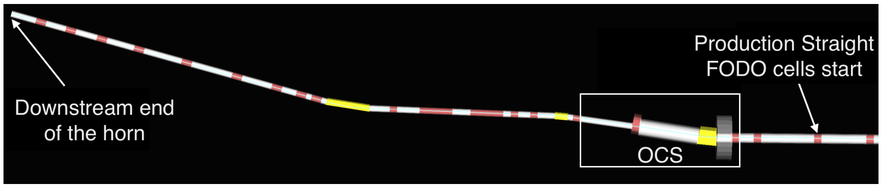

Figure 6

The G4beamline drawing from the downstream face of the horn to the FODO cells. Red: quadrupole, yellow: dipole, white: drift.

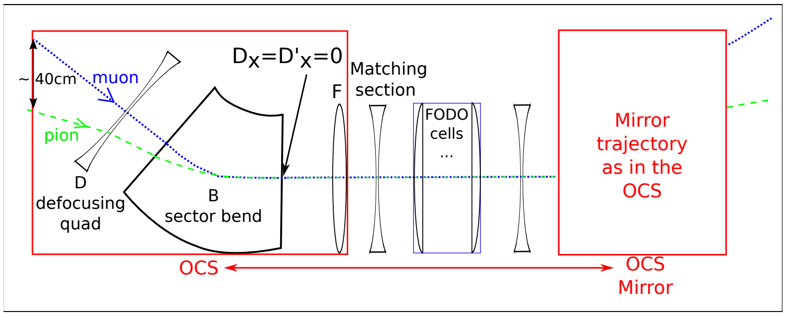

Figure 7

The schematic drawing of the injection elements.

A large dispersion, D_x, is required at the injection point, in order to achieve π and μ orbit separation which, for the OCS design, provides a 40 cm separation. A schematic drawing of the injection elements is shown in **Figure 7**. The sector dipole for muons in the OCS has an entrance angle for pions that is non-perpendicular to the edge, and the defocusing quadrupole in the OCS for muons is a combined-function dipole for the pions, with both entrance and exit angles non-perpendicular to the edges. The OCS will be followed by a short matching section to the decay ring FODO cells. The performance of the injection scenario was determining by calculating the number of muons at the end of the "production" straight (the decay ring straight along which the detector halls are placed, see Figure 4) using a G4beamline simulation. In this simulation, 0.012 muons per proton-on-target (POT) was obtained (see left panel of **Figure 8**). These muons have a wide momentum range (beyond that which the ring can accept, 3.8 GeV/c±10%) and thus will only partially be accepted by the ring. The green region in Figure 8 shows the 3.8±10% GeV/c acceptance of the ring, and the red region shows the high momentum muons which will be extracted by the OCS mirror at the end of the production straight, along with the pions that have not decayed ($\simeq$ 52%). Within the acceptance of the decay ring, approximately 0.008 muons per POT is delivered with this design. The muon beam at the end of the production straight ("first turn") is large, with $\sigma_{\mathrm{x,y}} \simeq 10$ cm. The right panel of Figure 8 shows the time structure of the muons, which is essentially the time structure of the protons in one bunch in the MI.

3.1. Decay ring

The nuSTORM decay ring design (94; 95) is a compact racetrack (480 m in circumference) based on large aperture (60 cm), separate function magnets (dipoles and quadrupoles). The ring is configured with FODO cells combined with Double Bend Achromat (DBA) optics. The ring layout, including the injection and extraction points (OCS and OCS mirror), primary proton beam absorber and the pion beam absorber, is illustrated in **Figure 9** and the ring design parameters are given in **Table 1**. With the 185 m length of the production straight, $\sim$ 48% of the pions decay before reaching the arc. Since the arcs are set for the central muon momentum of 3.8 GeV/c, the pions remaining at the end of the straight will not be transported by the arc, making it necessary to guide the remaining pion beam to an appropriate absorber. Another OCS, which is just a mirror reflection of the injection

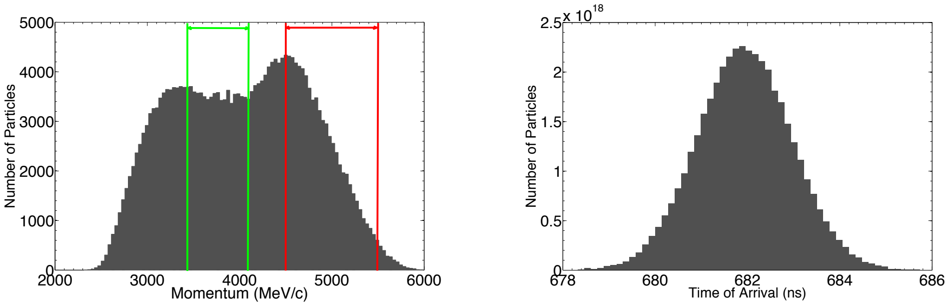

Figure 8

Left panel: The muon momentum distribution at the end of decay straight. The green band is the 3.8 GeV/c ± 10% acceptance of the ring. The red band indicates the muons that are extracted by the OCS mirror along with the pions. Right panel: Time structure of muons at the end of the decay straight.

OCS, is placed at the end of the production straight in order to extract the remaining pions towards the absorber. However, the OCS mirror extracts both the residual pions and muons which are in the same 5±0.5 GeV/c momentum range (see Figure 8). The pions are absorbed in the absorber, but these extracted muons can be used to produce an intense low-energy muon beam (see section 3.2). In addition to the FODO design described above, a decay ring for nuSTORM based on a racetrack, fixed-field, alternating-gradient (RFFAG) magnetic lattice, which could considerably increase (approximately by a factor of two) the neutrino flux, is also being considered (96–98).

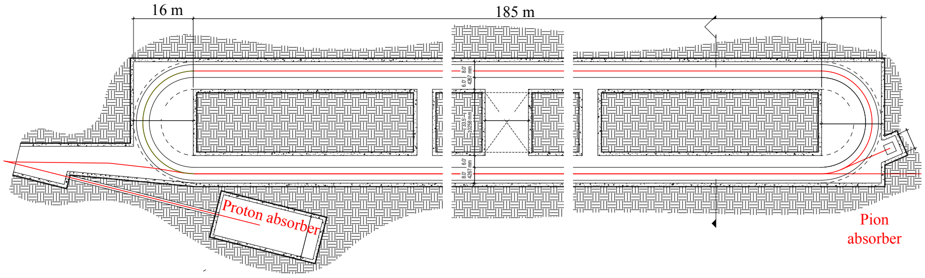

Figure 9

Racetrack ring layout. Pions are injected into the ring from the left. The pions and muons extracted at the end of the production straight are transported to the pion absorber shown in the figure. The residual proton beam absorber location is also shown.

3.2. Low-energy muon beam

In section 3, the OCS and its use for pion injection and extraction was described. As mentioned in that section, muons that are in the same momentum band (5 ± 0.5 GeV/c) at the end of the production straight will be extracted along with the pions by the mirror OCS. The beam absorber for pions can function as a muon “degrader”, if the absorber depth is appropriately chosen. An absorber depth of 3.5 m effectively absorbs all the

Table 1 Decay ring specifications

Parameter	Specification	Unit
Central momentum P_μ	3.8	GeV/c
Momentum acceptance	± 10%	Full width
Circumference	480	m
Straight length	185	m
Arc length	55	m
Beam pipe diameter	60	cm
Arc cell	DBA	
Ring Tunes (ν_x, ν_y)	9.72, 7.87	
Number of dipoles	16	
Number of quadrupoles	128	
Number of sextupoles	12	

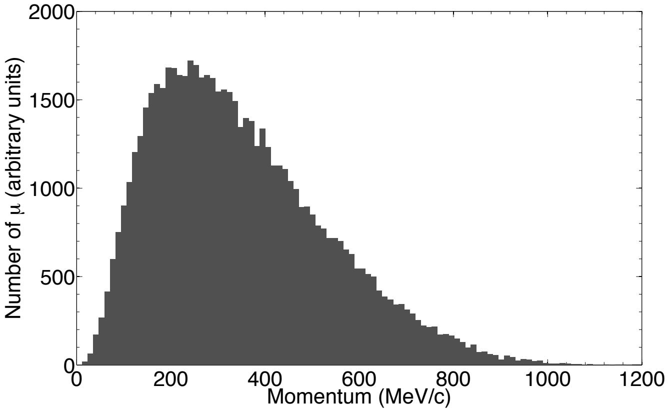

Figure 10

Momentum distribution of muons that exit the downstream face of the pion absorber

pions, while simultaneously functioning as a muon degrader to produce an intense, pulsed low-energy muon source. Results of a G4Beamline simulation are shown in **Figure 10** which presents the energy distribution of muons exiting the downstream face of this beam absorber. Approximately 10^{11} low-energy muons are produced per MI booster batch or $\simeq 1.2 \times 10^9$ per MI bunch (see Figure 8).

3.3. Beam Instrumentation

The goal of the beam instrumentation for nuSTORM is twofold. First, the instrumentation is needed in order to determine the neutrino flux at the near and far detectors with an absolute precision of $< 1\%$. Both the number of neutrinos and their energy distribution must be determined. If both the circulating muon flux in the storage ring is known on a turn-by-turn basis, and the orbit and orbit uncertainties (uncertainty on the divergence) are known accurately, then the neutrino flux and energy spectrum can be predicted with equal precision. The goals for the suite of beam instrumentation diagnostics for the nuSTORM decay ring are summarized below:

1. Measure the circulating muon intensity (on a turn by turn basis) to 0.1% absolute.
2. Measure the mean momentum to 0.1% absolute.
3. Measure the momentum spread to 1% (FWHM).
4. Measure the tune to 0.01.

Second, from the accelerator standpoint, in order to commission and run the decay ring, turn-by-turn measurements of the following parameters are crucial: trajectory, tune, beam profile and beam loss. The current estimate for these requirements is summarized in **Table 2** below.

Table 2 Decay ring instrumentation specifications for circulating muons ($\simeq 10^9$ per MI bunch

	Absolute accuracy	Resolution
Intensity	0.1%	0.01%
Beam position	5 mm	1 mm
Beam profile	5 mm	1 mm
Tune	0.01	0.001
Beam loss	1%	0.5%
Momentum	0.5%	0.1%
Momentum spread	1%	0.1%

3.3.1. Beam intensity. In order to measure the circulating muon intensities, one option is to use toroid-based Fast Beam Current Transformers (FBCT), such as the one recently developed at CERN for L4 (99). It consists of a one turn calibration winding and a 20-turn secondary winding, wound on a magnetic core and housed in a 4-layer shielding box. The mechanical dimensions will have to be adapted to the large beam pipe of nuSTORM. It should be noted that obtaining an absolute precision of 0.1% will be challenging, since problems associated with pulsed calibration and with electromagnetic interference (EMI) will influence the absolute accuracy of the FBCT. However, all components in the nuSTORM decay ring are DC, which will help with regard to EMI, but measurements on non-stable beams could become problematic. Demonstration of FBCTs operating with non-stable beams and not being affected by daughter particles from the decay is one of the few R&D tasks required for the technical implementation of nuSTORM. A combination of FBCT design, location along the beam line and within the decay ring and the application of shielding is the proposed R&D approach.

4. Detector design for the nuSTORM neutrino physics programs

Any of the multi-purpose detectors being considered as near detectors for the next generation of long-baseline experiments will meet the physics requirements for the detectors needed for the neutrino interaction physics program at the near hall at nuSTORM, or for the detector needed as part a short-baseline oscillation physics program and are described in detail in (100; 101). The far detector, at $\simeq 2000$ m, is used for the SBL neutrino oscillation physics studies and requires some special capabilities in order to maximize its performance

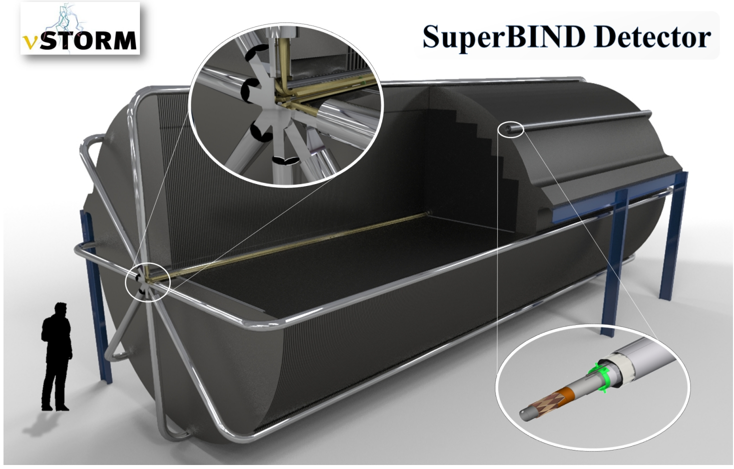

Figure 11

Far Detector concept. The left inset shows the central cryostat with eight return loops and the inset on the right is a detail of the Superconducting Transmission Line.

for searches in both the neutrino appearance and disappearance channels accessible at the nuSTORM facility.

The SBL element of the nuSTORM physics program would utilize the so-called "golden channel" (in Neutrino Factory parlance) where a neutrino oscillation appearance signal is given by the observation of a "wrong-sign" muon in the signal event. For example, with μ^+ stored in the ring (ν_e & $\bar{\nu}_\mu$ production), the oscillation of $\nu_e \to \nu_\mu$ can produce a ν_μ charged-current (CC) interaction in the detector that will have a μ^- in the final state, which is a muon of the wrong-sign from that expected from the CC interactions of the $\bar{\nu}_\mu$ in the beam. This detector needs to be magnetized in order to determine the sign of the muon. A magnetized iron detector similar to that used in MINOS was seen as the most straightforward and cost effective approach for the SBL oscillation physics. Thus, for the purposes of the nuSTORM oscillation physics, a detector inspired by MINOS (102), but with thinner plates and much larger excitation current (larger B field) was used as the baseline concept. The detector is an iron and scintillator sampling calorimeter called SuperBIND (1) (Super B Iron Neutrino Detector) and has a cross section of 6 m in order to maximize the ratio of the fiducial mass (1.3 kT) to total mass. The magnetic field will be toroidal, as in MINOS, and also used extruded scintillator for the readout planes. However, SuperBIND will use superconducting transmission lines to carry the excitation current and thus will allow for a much larger B field in the steel ($\approx$ 2T or greater over almost all of the steel plate). **Figure 11** gives an overall schematic of the detector. The Superconducting Transmission Line (STL) concept was developed for the Design Study for a Staged Very Large Hadron Collider (103), but recent cable-in-conduit superconductor development that has been carried out for ITER (104–106) will be applicable to the SuperBIND design. Minimization of the muon charge mis-identification rate requires the highest field possible in the iron plates, thus SuperBIND requires a much larger (240 kA-turns) excitation current than even that of the MINOS near detector (40 kA-turns). The excitation circuit for SuperBIND consists of eight turns, each carrying 30 kA (see the insets of Figure 11).

5. Performance of the nuSTORM facility – Neutrino physics

The reach of the neutrino physics that can be done at the nuSTORM facility is determined, to a large degree, by the quality of the neutrino beams it produces. The nuSTORM facility provides bright, flavor-pure beams that can be precisely characterized by beam instrumentation in the pion transfer line and in the decay ring. This is what sets nuSTORM apart from other neutrino sources, giving it many of the qualities of a photon light source (accurate flux and energy determination). The physics program that can be done at the near hall at nuSTORM is identical to that being proposed at the near sites of planned future long-baseline oscillation experiments (T2HK and LBNE, for example) and could use similar, if not identical, detector systems. However with respect to neutrino interaction physics, nuSTORM provides large samples of ν_e and $\bar{\nu}_e$ beams as well as nearly flavor-pure ν_μ and $\bar{\nu}_\mu$ beams. For the short-baseline oscillation physics performance, nuSTORM takes advantage of the "golden channel" (appearance) mentioned above, as well has having access to the $\overset{(-)}{\nu}_\mu$ disappearance channels. The $\overset{(-)}{\nu}_e$ appearance and disappearance channels would be most effectively studied with a magnetized totally active detector such as LAr.

5.1. Neutrino beams produced at nuSTORM

As mentioned in section 1, the neutrino beams produced at nuSTORM can be determined with excellent precision with the use of conventional beam diagnostic instrumentation to understand the parent particle distributions, from which the neutrino flux can then be precisely calculated. In the sections that follow, we describe the neutrino beams expected from the facility (107), indicating the overall flux (normalized to 10^{21} protons on target), neutrino flavor composition and expected bin-to-bin errors.

5.1.1. Neutrino flux from pion beam. Although the design-case of nuSTORM is to produce neutrinos from muon decay, the neutrino beam from pion decay in the production straight produces a very intense $\overset{(-)}{\nu}_\mu$ beam. In order to quantitatively investigate this beam, an ensemble of particles produced in a MARS (108) simulation of the target and horn were tracked using G4Beamline from the downstream face of the horn and then through the transfer line and injection into the decay ring via the OCS. After tracking through the transfer line, the pion beam was sampled at fifty locations along the production straight to yield an ensemble of pions representative of the beam. To obtain the muon ensemble, the pions were allowed to decay and the muons sampled at the end of the production straight, weighted for the momentum acceptance of the ring.

The sampling of the particles' energy and momenta in the G4Beamline tracking could then be used to calculate (from decay kinematics) the neutrino flux at arbitrary locations, or G4Beamline could be used to simulate the production of the neutrino beam itself. It was considered that this sampling is analogous to the information of the beam obtained from standard diagnostic instrumentation.

The simulated flux from a π^+ beam, which included all particle types transported from the target to the ring (pions, kaons, muons), at the near detector can be seen in **Figure 12** (left) and at the 2 km far detector in Figure 12 (right) where, due to the statistical limitations of the full G4Bealine tracking to observe suppressed decay branches, the flux was calculated from the pion and kaon distributions, allowing for all possible decay branches. As can be seen in the figures, nuSTORM produces a ν_μ beam of unmatched purity. Although not seen in Figure 12, the simulation did include the neutrino flux from

$K^+ \to \nu_e, \pi^- \to \bar{\nu}_\mu$ and $\pi^+ \to \nu_e$. Their contribution to the flux was too small to be seen on the scale shown in the figure.

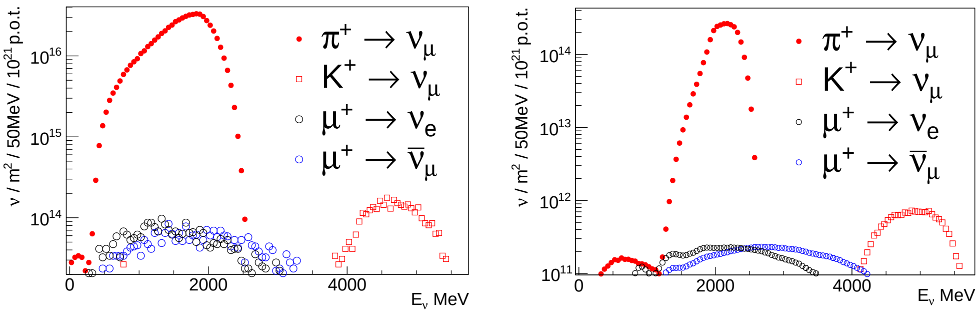

Figure 12

Neutrino flux from π^+ beam at the near detector (left) and at the far detector (right)

5.1.2. Muon beam. Using the same methodology of simulating the particle trajectories of the pions within the decay straight, a sample of muons was obtained from which the neutrino flux at arbitrary detector locations could be determined. The errors on the binned flux are dependent solely on the knowledge of the particle trajectories obtained by the beam diagnostics. A combination of instrumentation performance predictions and simulations imply that the bin errors will be below 1%, as detailed in **Table 3**.

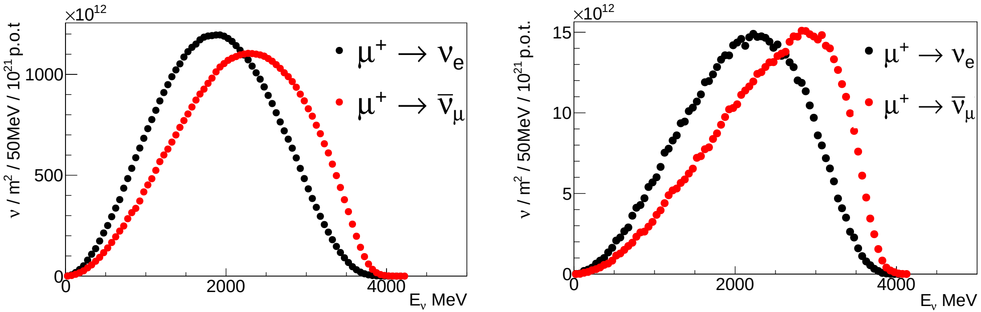

Figure 13

Neutrino flux from μ^+ decay at the near detector (left) and at the far detector (right)

The simulated flux from the stored μ^+ beam can be seen for the near detector in **Figure 13** (left) and the 2km far detector in Figure 13 (right).

5.1.3. Neutrino flux precision. The precision of the flux estimates is affected by a number of factors, including: understanding and stability of the magnetic lattice; the overall flux of and type of particles transported by the lattice; and the momentum distributions of those particles. Given the time structure of the beam and the bunch intensity, in the absence of particle decays, beam-current transformers can measure the circulating beam intensity (or in the case of pions, the intensity in the production straight) to a precision approaching 0.1%. Determining, quantitatively, the effects of particle decays on the BCTs is work that still needs to be done and is considered one of the few R&D tasks needed in order to

Table 3 Flux uncertainties expected for nuSTORM.

Parameter	Uncertainty
Intensity	0.3%
Divergence	0.6%
Energy spread	0.1%
Total	$\lesssim$1%

Table 4 Event rates at 50 m from the end of the decay straight per 100T for 10^{21} POT.

μ^+ stored Channel	**k**Events	μ^- stored Channel	**k**Events
ν_eCC	5,188	$\bar{\nu}_e$CC	2,519
$\bar{\nu}_\mu$CC	3,030	ν_μCC	6,060
ν_eNC	1,817	$\bar{\nu}_e$NC	1,002
$\bar{\nu}_\mu$NC	1,174	ν_μNC	2,074
π^+ injected Channel	**k**Events	π^- injected Channel	**k**Events
ν_μCC	41,053	$\bar{\nu}_\mu$CC	19,939
ν_μNC	14,384	$\bar{\nu}_\mu$CC	6,986

Table 5 Event rates due to charge current interactions at 2 km per 1.3 kT for 10^{21} POT.

μ^+ Stored		
Channel	No Oscillation	Oscillation
$\nu_e \rightarrow \nu_\mu$	0	288
$\nu_e \rightarrow \nu_e$	188,292	176,174
$\bar{\nu}_\mu \rightarrow \bar{\nu}_\mu$	99,893	94,776
$\bar{\nu}_\mu \rightarrow \bar{\nu}_e$	0	133
π^+ Stored		
Channel	No Oscillation	Oscillation
$\nu_\mu \rightarrow \nu_\mu$	915,337	854,052
$\nu_\mu \rightarrow \nu_e$	0	1,587

implement nuSTORM. In order to investigate the effect of a measurement error on the divergence of the muons stored in the ring, the muon divergence of each particle in the muon beam was inflated by 2% and the resulting flux compared to the nominal divergence. The mean difference in the flux in 50 MeV energy bins based on a 2% error in the divergence of the primary beam was determined to be $\simeq 0.6\%$.

5.1.4. Rates. Based on the flux calculations given above, the number of neutrino interactions expected from a total exposure of 10^{21} POT was calculated and is given in **Table 4** for a 100 T detector at 50 m. **Table 5** gives the number of charge current interactions in the far detector (1.3 kT fiducial mass) for a null-oscillation assumption and for the case where a 3 + 1 model with the LSND/MiniBooNE best fit parameters is assumed.

5.2. nuSTORM's sensitivity to sterile neutrinos

The nuSTORM facility provides the opportunity to perform searches for sterile neutrinos with unmatched sensitivity and breadth. In this section, we review the analysis for the $\overset{(-)}{\nu}_\mu$ appearance and disappearance channels that was performed using the beams (μ^+ stored) from nuSTORM normalized to 10^{21} POT and using the SuperBIND detector described in the previous section. The performance estimates are based on a detailed simulation in which neutrino events in SuperBIND were generated using GENIE (version 2.8.4) (109). The interaction products were propagated through the detector using GEANT4 (version 10.00) (110) and the resulting energy deposition was smeared with a simple digitization algorithm and clustered into hits. Finally, a reconstruction optimized for the identification of muon tracks associated with neutrino charge current interactions was applied to the digitized simulation.

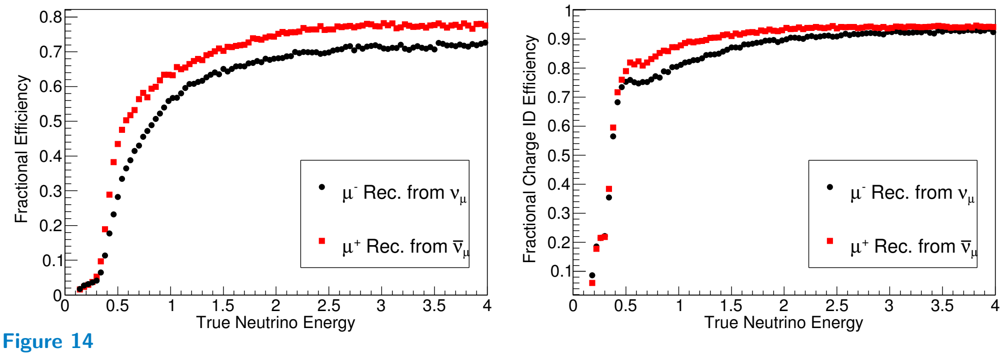

Figure 14

Reconstruction (left) and charge identification (right) efficiencies for muons generated from charge current neutrino interactions in SuperBIND, at typical nuSTORM energies.

The reconstruction used a simple geometric approach to identify potential tracks and a Kalman filter algorithm to extend the track to the event vertex and to fit for the curvature (111). The pattern recognition algorithm first identified planes with single points of energy deposition. After the tracks were identified they were passed to the fitting algorithm. The reconstruction and charge identification efficiency of this algorithm is shown in **Figure 14** for muon neutrino charge current interactions in SuperBIND. The algorithm continues to operate until it cannot find an instance of five or less isolated clusters in the event. The longest trajectory identified by this algorithm was associated with the muon track.

In the reconstruction, a number of events will be identified with the incorrect charge either from failures in the reconstruction algorithm or from pions which are misidentified as muons. The fractional occurrence of such events is the complement of the charge identification efficiency shown in Figure 14. Such tracks are the primary background for the identification of muon-flavored charge current neutrino interactions in both the wrong sign appearance and disappearance channels. The analysis shown here utilized the Toolkit for Multi-Variate Analysis (TMVA) (112) included as part of the ROOT package (113). This analysis takes five variables as input to produce a figure of merit which can be used to identify signal from background.

After training, the analysis was optimized for signal significance assuming an initial sample size of signal and background events calculated using the GLoBeS program (114) with sterile neutrino parameters derived from recent global fits (65) to short baseline appearance data input assuming a 3+1 sterile neutrino model.

5.2.1. Sterile neutrino oscillation physics with muon neutrinos -Appearance and disappearance channels. The optimization of the muon neutrino appearance channel was conducted using the significance statistic $S/\sqrt{S+B}$ where S is the total number of selected signal events and B is the number of background events selected. Several different multi-variate methods were tested for this analysis, but it was determined that the Boosted Decision Tree (BDT) method produced the best result. The fraction of events that survived the application of the BDT analysis on sets of neutrino CC and NC events, as a function of the true neutrino energy, is shown in **Figure 15**. The resultant signal efficiency is reduced in this optimization in order to reduce the background below a few parts in 10^4 level. This

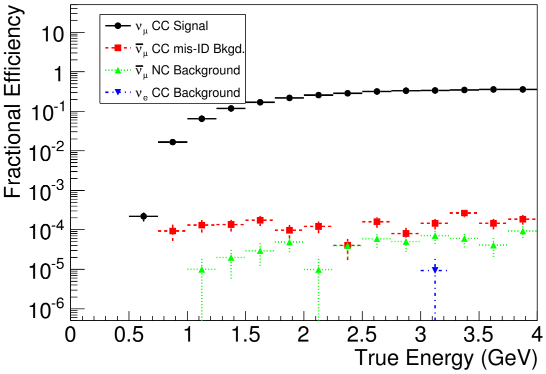

Figure 15

Event selection efficiency of the optimized boosted decision tree analysis for SuperBIND, at the energies available to the nuSTORM facility.

degree of background suppression is what allows for a measurement in this channel with a potential for 10σ sensitivity.

The sensitivity for $\nu_e \to \nu_\mu$ (the CPT invariant channel of the LSND/MiniBooNE signal) was determined within the GLoBeS framework. The simulation provided the detector response, as characterized in a "migration matrix" that maps the true neutrino interaction rates to reconstructed neutrino rates, including both efficiency and resolution effects. The migration matrix was then used as input to the GLoBeS program. The signal (ν_μCC) response was evaluated with the background (ν_eCC, $\bar{\nu}_\mu$CC, $\bar{\nu}_\mu$NC) response and the number of events in each associated channel was evaluated for the potential values of Δm_{14} between 0.03 and 30 eV^2 and $\theta_{e\mu}$ between 10^{-6} and 0.1. A representation of the deviation from the null-oscillation hypothesis was then calculated using a χ^2 statistic for each point and the result then used to map out the sensitivity shown in **Figure 16**. This sensitivity has been plotted with contours determined from global fits, shown in Figure 2, to the existing short baseline oscillation appearance data including LSND, MiniBooNE, ICARUS, and MINOS. The 10σ significance contour demonstrates that the ν_μ appearance measurement alone will provide a definitive statement regarding the existence of a sterile neutrino in the region consistent with the combination of the fit to the LSND, MiniBooNE, gallium, and reactor data. Further measurements serve to refine these results.

The muon disappearance channel used a similar analysis with a different optimization. The disappearance measurement is an analysis of the spectrum shape, so a pure counting statistic is insufficient. A χ^2 was adopted as a figure of merit to determine the largest separation between the null hypothesis and a test case during optimization before compiling the sensitivity curves of Δm_{14} vs. $\theta_{\mu\mu}$ shown in **Figure 17**, where

$$\sin^2 2\theta_{\mu\mu} = 4|U_{\mu 4}|^2(1 - |U_{\mu 4}|^2). \qquad (2)$$

These curves were again compiled using GloBeS with the response from the signal ($\bar{\nu}_\mu$ CC) and background ($\bar{\nu}_\mu$ NC and ν_e CC) simulations. The 99% confidence limits from the disappearance measurement with a muon decay source can provide an improvement over the limits from existing data for Δm^2_{14} greater than 0.3 eV^2. Assuming a total systematic

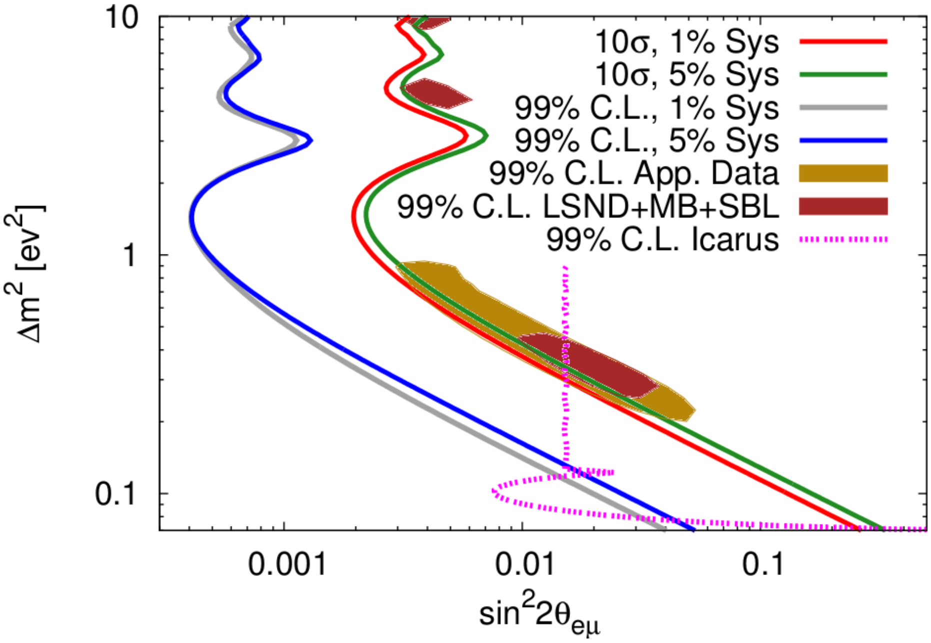

Figure 16

The sensitivity of a ν_μ appearance experiment to a short baseline oscillation due to a sterile neutrino, assuming a 3+1 model. Both the 10σ significance and 99% confidence level contours are shown for two different scenarios for the systematic uncertainties; one in which the total systematic uncertainty is 1% of the beam normalization and a second when the systematic uncertainty is 5%. The 99% contour generated from the fit to the MiniBooNE and LSND experiments with the Gallium and Reactor anomalies is shown by the areas filled brown, while the fit to all available appearance data is shown with the tan filled area. The recent 99% exclusion contour from Icarus is also shown.

uncertainty of 1%, nuSTORM has the potential for a discovery with a 5σ significance in the region allowed by the current exclusion limits.

The ν_μ flux from pion (π^+ injected) decay generated is 13 times greater than the neutrino flux from muon decay in nuSTORM and has a very different energy distribution. The information provided by the ν_μ disappearance channel is complementary to the $\bar{\nu}_\mu$ disappearance channel. The ν_μ disappearance experiment was simulated using an optimization similar to that of the $\bar{\nu}_\mu$ disappearance experiment and the neutrino flux shown in Figure 12. The contour showing the 5σ confidence level for a measurement at nuSTORM with this pion neutrino source as a function of Δm^2_{14} *vs.* $\sin^2 2\theta_{\mu\mu}$ is shown in Figure 17 (right). Because of the narrower energy distribution in the pion source, there is a larger variation in the limits as a function of Δm^2_{14}. However there is still potential for improvement over existing limits for a large subset of Δm^2_{14} greater than 0.3 eV^2.

5.2.2. Global fits to the muon neutrino channels. The combination of the disappearance and appearance measurements is an important feature of nuSTORM, as measurements of multiple channels can be made simultaneously. A fit using the combination of the signal channels such as the ν_μ appearance and $\bar{\nu}_\mu$ disappearance channel from the muon decay

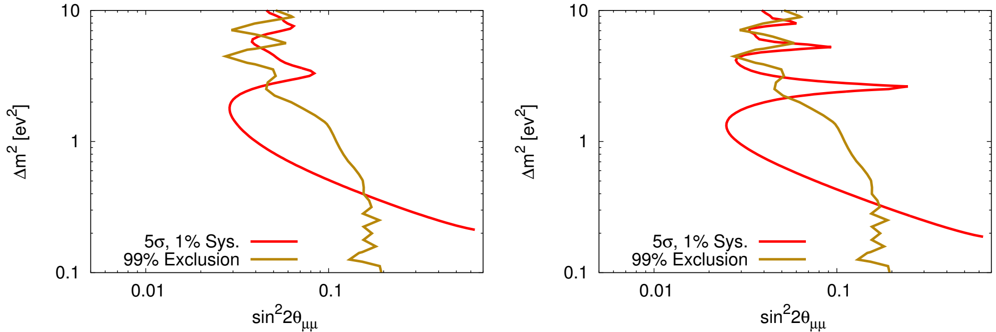

Figure 17

The sensitivity of a $\bar{\nu}_\mu$ from μ^+ decay (left) and a ν_μ from π^+ decay (right) disappearance experiment to a SBL oscillation due to a sterile neutrino assuming a 3+1 model. The 5σ contour for the disappearance experiment assuming a 1% systematic is shown along with the 99% exclusion limit derived from the existing disappearance oscillation data.

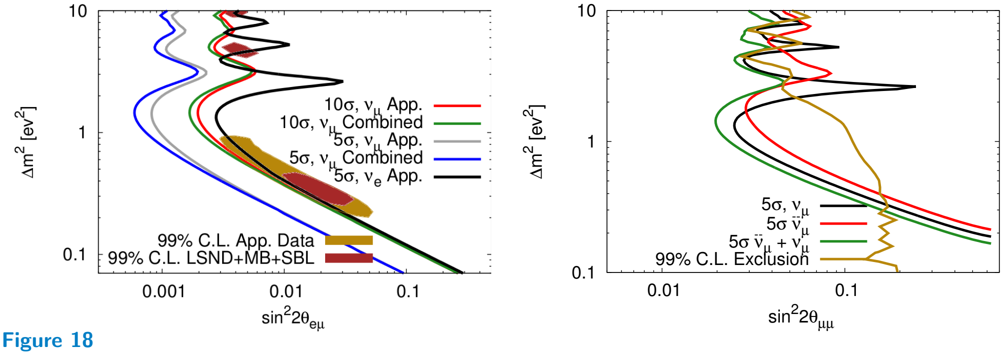

Figure 18

Sensitivities of combinations of experiments at nuSTORM to short baseline oscillations associated with a sterile neutrino assuming a 3+1 model. Left: the combination of ν_μ appearance and disappearance experiments expressed in terms of the effective mixing angle $\theta_{e\mu}$. Included is the 5σ contour derived from the electron neutrino appearance data from the pion beam source. Right: the sensitivity of the ν_μ disappearance experiment from the pion decay source and the $\bar{\nu}_\mu$ disappearance experiment from the muon decay source as 5σ significance contours. The sensitivity of the combination of the experiments is shown with the green line.

source and the ν_μ disappearance channel from the pion decay source is allowed because the channels are not statistically correlated; any correlation between individual events because of a shared source decay is lost due to the low neutrino interaction rate.. The channels from the muon decay source are separated by charge and the pion decay source is separated from the muon decay source by time. This additional information reduces the number of assumptions required by the fit to the data for a given sterile-neutrino model. The improvement in the measurement of $\theta_{e\mu}$ and $\theta_{\mu\mu}$ from the combination of multiple channels is shown in **Figure 18**. The addition of disappearance information produces an improvement in the appearance sensitivity at $\Delta m^2_{14} \sim 1$ eV^2, but minimal improvement in the region preferred by existing measurements. In contrast, the addition of the appearance measurement makes a minimal contribution to contours in the $\theta_{\mu\mu}$ plane while the combination of the two disappearance measurements results in a substantial increase in the coverage.

5.2.3. Sterile neutrino oscillations with electron neutrinos. Although a strong case can be made for nuSTORM using just the muon neutrino oscillation physics, it is also important to measure oscillations to electron neutrinos to evaluate the consistency of any measurement. SuperBIND is not optimized for the measurement of electron-neutrino interactions, since single electrons can not be resolved for charge identification, nor may the interaction vertex be positively inferred. However an electron shower may be observed in SuperBIND and a figure of merit may be defined based on the distribution and extent of photo-electrons observed in the detector, which can differentiate (with high purity) electron neutrino interactions from neutral current interactions (which are the leading background). To achieve this high purity, hard cuts were imposed on the the observed shower shape and deposited charge, such that the detection efficiency for electron neutrino charge current events is reduced to 10%. The corresponding neutral current background rejection factor is 99.7%. The cut on the figure of merit was tuned to minimize the number of NC events identified as electron neutrino CC events, while maintaining a high enough ν_e CC efficiency to produce a useful number of candidate events. Of the three electron neutrino oscillation channels, only the $\nu_\mu \to \nu_e$ channel available from the pion decays may produce a significant measurement in SuperBIND, based on these efficiencies.

In the context of the pion sourced neutrino beam, the backgrounds for the $\nu_\mu \to \nu_e$ appearance channel are from unoscillated ν_μ as well as from $\bar{\nu}_\mu$ and ν_e from muon decays in the first 6 ns after injection. The $\overset{(-)}{\nu}_\mu$ CC interactions may be clearly distinguished from NC interactions by the presence of a muon, so a further suppression of more than an order of magnitude may be expected over the above electron neutrino selection. There is nothing to distinguish the beam ν_e from the oscillated ν_e, so no further suppression is possible for this background. Even so, a 5σ measurement may be made in the region favored by the LSND and MiniBooNE data as shown in Figure 18 (left). This will not make a substantial contribution to the global fit of the nuSTORM channels because of its relatively low overall significance.

Given that the experiment is not limited by systematic uncertainties in the beam composition, great gains in $\overset{(-)}{\nu}_e$ appearance measurements can be made with increased detector resolution and efficiency. A more significant measurement of short baseline ν_e appearance from pion decays may be possible with a greater signal efficiency for ν_e CC interactions with better background rejection. To achieve the 10σ significance observed in the ν_μ appearance, the background must be suppressed by a factor of 10^{-4} with respect to the signal. Once such a suppression factor is achieved along with a modest increase in efficiency, a measurement from $\bar{\nu}_\mu \to \bar{\nu}_e$ appearance (generated by muon decays) may also be achieved, producing a simultaneous measurement of appearance in both neutrino charge states, similar to what is achieved with the muon neutrino disappearance. The required 10^{-4} background suppression can only be achieved in a magnetized, totally active detector with strong particle identification capabilities. The strongest candidate technology is a magnetized liquid argon TPC, although it has not yet been demonstrated that the particle and charge identification capability of such a detector will provide the required background rejection (115). We make note that, if the existence of a light-sterile neutrino is confirmed, CP violation in a 3+1 scenario might be observable in a nuSTORM-like facility (116), especially if $\overset{(-)}{\nu}_e$ and $\overset{(-)}{\nu}_\mu$ appearance and disappearance channels are accessible. A magnetized liquid argon TPC has the potential to make this possible.

5.2.4. Systematics. The experimental sensitivity obtainable at the nuSTORM facility from muon decays uses the systematic uncertainties shown in Table 6. These systematic uncertainties are motivated by the exceptionally low beam uncertainties (see section 5.1 and expected improvements in the measurements of neutrino cross-sections. With these uncertainties, the expected interaction physics uncertainty is only limited by the detector performance. An upper limit on the potential systematic uncertainty is given based on the existing estimates of systematic uncertainties reported by MINOS. To illustrate the effect that this would impose on results from nuSTORM, the systematic uncertainties were inflated by a factor of 5 to produce the "5%" contours shown in Figure 16. Increasing the systematic uncertainty in this way has a minimal impact on the measurements of the ν_μ appearance due to the small number of background events surviving selection. Similarly, the significant backgrounds allowed for the disappearance measurements mean that the systematic uncertainties have a large impact on the disappearance measurements.

Table 6 Systematic uncertainties expected for a short-baseline muon neutrino appearance experiment based at nuSTORM.

Uncertainty	Expected Contribution	
	Signal	Background
Flux	0.5%	0.5%
Cross section	0.5%	5%
Hadronic Model	0	8%
Electromagnetic Model	0.5%	0
Magnetic Field	0.5%	0.5%
Variation in Steel Thickness	0.2%	0.2%
Total	1%	10%

6. Path to a muon collider

6.1. Introduction

Muons for a muon collider (117–122) or neutrino factory (4; 122) are produced as a tertiary beam: protons are directed onto a target to yield a beam of pions which are then captured in a high-field solenoid and allowed to drift and decay into muons. As a result, the muon beam has a very large phase space size, commonly referred to as "emittance". Reducing the emittance of the beam ("cooling" the muon beam) is required in order to reach an acceptable level of performance for the muon collider and, for the neutrino factory, can give up to a factor of three increase in the neutrino flux. Given that muons have a relatively short life span (2.2 μs in the rest frame), ionization cooling (123–125) is deemed to be the only technique fast enough to cool a muon beam without excessive loss due to decay.

6.2. Ionization cooling overview

Various aspects of muon ionization cooling were actively studied over the last two decades, first by the Neutrino Factory and Muon Collider Collaboration (NFMCC) (126) and later by the Muon Accelerator Program (MAP) (127–130). Muon-based accelerator facilities have the potential to discover and explore new fundamental physics, but require the development of demanding technologies and innovative concepts. One of these is muon ionization cooling.

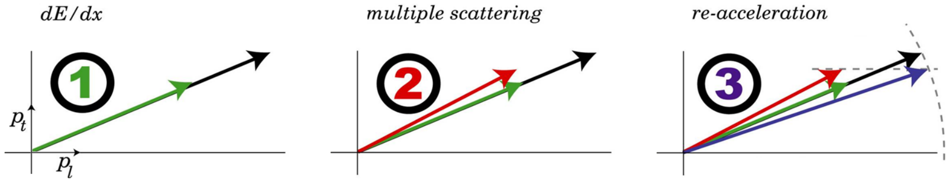

Figure 19

Ionization cooling principle. p_t and p_l are the transverse and longitudinal muon momentum, respectively. Left plot: all components of momentum are reduced in material, green arrow is the reduced momentum. Central plot: multiple scattering in material increases the angular spread of the particles, red arrow. Right plot: longitudinal momentum is restored in RF cavities, red to purple arrow transition. The overall effect is the transition from the black arrow to the purple arrow, the beam spread is reduced.

We will briefly review muon ionization cooling starting with the fundamentals of transverse cooling. Transverse cooling is achieved by letting a beam of muons pass through an absorber in which all components of each particle's momentum are reduced (**Figure 19**, left panel, black to green arrow). The longitudinal momentum is then restored in a set of RF cavities. If the absorber material and optics parameters are chosen carefully, the net effect is a reduction in the transverse emittance. However, multiple scattering in the absorber material also occurs which increases the phase space, as shown schematically in the middle panel of Figure 19 (green arrow to red arrow). After application of the RF, the red arrow becomes the purple arrow (Figure 19, right panel) showing a reduction in the transverse phase space. The amount of cooling is described by the following formula:

$$\frac{d\epsilon_n}{dz} \approx -\frac{1}{\beta^2}\left\langle \frac{dE_\mu}{dz} \right\rangle \frac{\epsilon_n}{E_\mu} + \frac{1}{\beta^3}\frac{\beta_\perp E_s^2}{2E_\mu mc^2 X_0}, \tag{3}$$

where $\beta = v/c$, ϵ_n is the normalized emittance ($\epsilon_n = \beta\gamma\epsilon$, γ is the Lorentz factor, ϵ is the geometric emittance characterizing the size of the beam in phase space), z is the path length, E_μ is the muon beam energy, X_0 is the radiation length of the absorber material, and E_s is the characteristic scattering energy. $\beta_\perp$ is the betatron function that relates the beam width at the location s along the nominal beam trajectory to its emittance via $\sigma(s) = \sqrt{\epsilon \cdot \beta_\perp(s)}$.

In Equation 3 two competing effects can be seen: the first term is the cooling (reduction of phase space beam size) component from ionization energy loss and the second term is heating (increase of phase space beam size) from multiple scattering. That last term can be minimized by reducing $\beta_\perp$ (by placing the absorber at a minimum of the betatron function), and by choosing a low-Z material to increase X_0. The "equilibrium emittance" is the point in the cooling channel where the normalized emittance no longer changes ($\frac{d\epsilon_n}{dz} = 0$) and can be shown to be approximately:

$$\epsilon_n^{(eq.)} \approx \frac{\beta_\perp (0.014)^2}{2\beta m_\mu \frac{dE_\mu}{dz} X_0}. \tag{4}$$

Six-dimensional (6D) cooling, reducing both the transverse and longitudinal sizes of the beam, results in the best quality beam. In order to reduce the longitudinal emittance, the so-called "emittance exchange" technique is commonly used, where a dispersive beam is passed through a discrete or continuous absorber in such a way that high-energy particles traverse more material than low-energy particles. The net result is a reduction of the longitudinal emittance at the cost of simultaneously increasing the transverse emittance. By controlling the amount of emittance exchange, the six-dimensional emittance can be reduced.

Muon colliders require a six order of magnitude reduction in the muon beam phase space, while a neutrino factory benefits from the cooling. Various scenarios were recently put forward by the Muon Accelerator Staging Study (MASS) (131; 132), and for each of those scenarios there are corresponding cooling channel options based on vacuum RF or high-pressure gas-filled RF that can reach the desired design parameters.

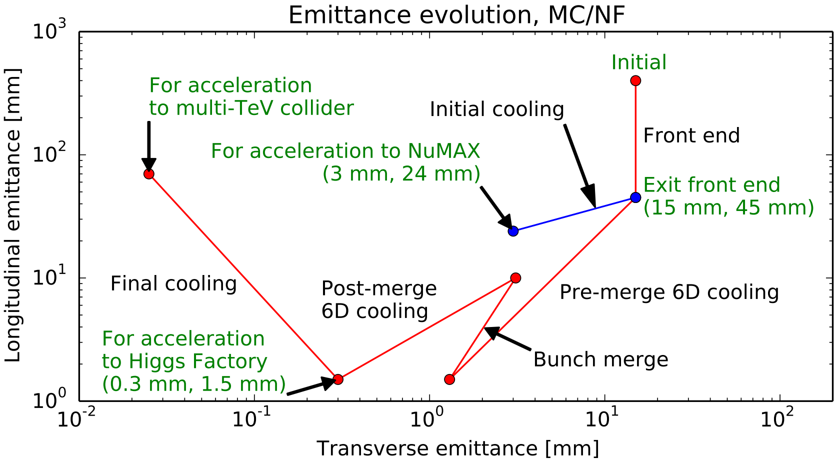

Figure 20

Emittance evolution for different applications. Blue line: NuMAX neutrino factory, red line: muon collider options.

Figure 20 shows the evolution of the transverse and longitudinal normalized emittances in a cooling channel that uses vacuum RF, see below. The blue line corresponds to the cooling needed for the neutrino factory design, NuMAX (131; 132). The cooling process starts in the top-right corner of the diagram where the beam comes out of the muon front end (after RF bunching) with a transverse normalized emittance of 15 mm (transverse beam size $\sigma_\perp = 8$ cm), and longitudinal emittance of 45 mm (longitudinal beam size $\sigma_\parallel = 15$ cm). Twenty-one bunches selected by the front end are cooled in the pre-merge channel, followed by the bunch merge section combining all bunches into one. The resulting single bunch is then cooled further in the post-merge cooling channel, until the Higgs Factory muon collider design emittances of 0.3 mm transverse (beam size $\sigma_\perp = 2$ mm) and 1.5 mm longitudinal (beam size $\sigma_\parallel = 21$ mm) are reached. A multi-TeV collider will also require a final transverse cooling section (which increases the longitudinal emittance) in order to reach the design luminosity.

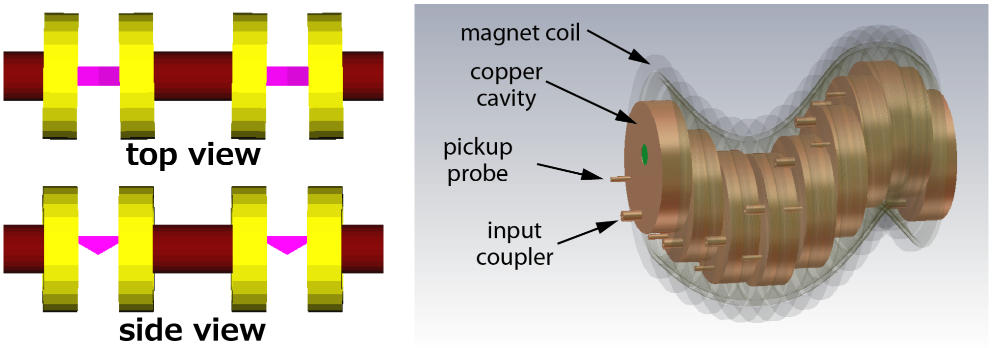

Figure 21

6D cooling channels. Left panel: Schematics of one of the stages of the VCC. Yellow: magnetic coils for focusing and dispersion generation, red: RF cavities for replenishing the energy lost in the absorbers, magenta: solid LiH or liquid hydrogen, depending on the stage. Right panel: Conceptual design of the helical cooling channel. RF cavities inside the magnetic coils are shown. Magnetic coils are semi-transparent.

6.3. 6D cooling channels

The front end of a muon facility (either a muon collider or neutrino factory) has been optimized (133) to maximize the number muons collected (μ^+ and μ^- are captured and transported simultaneously in a system of solenoids) in the momentum range of 100–300 MeV/c. It is in this momentum range that the initial stages of ionization cooling are most effective. It is also a regime where the number of muons captured per POT is quite high. For example, the current benchmark for the muon front end is $\simeq 0.1$ μ^+ in the momentum range of 100–300 MeV/c, per POT. In comparison, as was stated in section 3, nuSTORM collects $\simeq 0.008$ μ^+ in the ~ 0.8 GeV/c momentum acceptance of the ring, per POT. In the following two sections, we give an overview of two scenarios that have been shown to achieve the required 6D cooling necessary for the muon collider.

6.3.1. Vacuum cooling channel.

In the vacuum cooling channel (VCC), each cell consists of solenoids for focusing that are tilted slightly to generate bending and dispersion, wedge-shaped absorbers where cooling takes place, and vacuum RF cavities to replenish the energy lost in the absorbers. The channel is tapered by changing the geometry of the lattice (magnetic field strength, RF frequency, absorber opening angle) progressively (134) to keep emittance away from the equilibrium thus improving cooling efficiency. The layout of one of the latter stages is shown in the left panel of **Figure 21**.

This scheme uses separate 6D ionization cooling channels for the two signs of the particle charge. In each, a channel first reduces the emittance of a train of muon bunches until they can be injected into a bunch-merging system. The single muon bunches, one of each sign, are then sent through a second 6D cooling channel where the transverse emittance is reduced as much as possible and the longitudinal emittance is cooled to a value below that needed for the collider. The beam can then be recombined and sent though a final cooling channel using high-field solenoids that cools the transverse emittance to the required value for a multi-TeV collider, while allowing the longitudinal emittance to grow.

The performance of the vacuum cooling channel was simulated using G4Beamline, and after a distance of 490 m (80 stages) the 6D emittance is reduced by a factor of 1000 with a transmission of 40%. Decreasing the longitudinal emittance below 1.5 mm leads to severe particle loss and emittance growth due to space charge effects. Thus, after reaching this threshold, the beam is cooled in the transverse direction only. The simulated results are in agreement with theoretical predictions (135). Finally, a transverse emittance of 280 μm can be achieved, which is below the baseline requirement for a muon collider after the final 6D cooling sequence.

6.3.2. High-pressure gas-filled cooling channel. An alternative to the VCC is a homogeneous ionization absorber filled helical cooling channel (HCC) (136–138). The primary magnetic components in the HCC are the solenoid and counteracting helical dipole to define the reference trajectory and the helical dipole gradient that controls the dispersion and provides transverse stability. The right panel of Figure 21 shows the conceptual design of the helical cooling channel. High-pressure hydrogen gas filled RF (HPRF) cavities are embedded inside the magnetic coils in the HCC. RF cavities are placed continuously along the helical beam path in the HCC magnet. High-pressure hydrogen in the cavity acts as a homogeneous ionization absorber. It also reduces the probability of electric breakdown in the RF cavity and allows higher operating E fields in strong magnetic fields. The breakdown suppression model has been experimentally verified and no RF degradation due to the external magnetic field has been observed (139). The ultimate equilibrium emittances that can be reached are 0.6 mm in transverse direction, and 0.9 mm in the longitudinal direction, which could be translated into the desired values by using emittance exchange.

6.4. 6D cooling tests

As mentioned above, muon ionization cooling improves the stored-muon flux at the neutrino factory and is absolutely crucial for a muon collider of any center-of-mass energy in order to achieve the required luminosity. The Muon Ionization Cooling Experiment (MICE) (140; 141) will study four-dimensional ionization cooling and work is underway to specify the scope of a follow-on six-dimensional (6D) cooling experiment. MICE is a “single-particle” experiment; the four-momenta of single muons are measured before and after the cooling cell and then input and output beam emittances are reconstructed from an ensemble of single-muon events. For 6D cooling, an experiment with a high-intensity pulsed muon beam is preferred. One feature of nuSTORM is that an appropriate low-energy muon beam with these characteristics can be provided in a straightforward fashion (see section 3.2).

Thus, one of the key 6D cooling channel designs described in the previous sections can be tested at the nuSTORM facility without affecting the main neutrino physics programs. nuSTORM provides a low-energy muon source (see Figure 10) with significant intensity ($\approx 10^{10}\mu$/pulse in the 100–300 MeV/c momentum range). This beam can be produced simultaneously with the neutrino physics program at little additional cost. This is possible because nuSTORM requires an absorber to absorb pions remaining (about 50% of those injected into the ring) after the first straight. Pions in the momentum range 5 GeV/c ±10% are extracted to the absorber along with many muons in the same momentum window (forward decays). The absorber will act as a degrader for these muons, producing the desired low-energy muon beam. This is achieved by choosing the length of the degrader to be 3.54 m of iron.

Once the bench test for the cooling channel is carried out with no beam, a section of the cooling channel long enough for appreciable 6D cooling could be used at the nuS-

TORM facility for a demonstration with beam. The corresponding study and simulation are underway.

7. Muon accelerator staging study (MASS): rationale for a staged approach

The feasibility of the technologies required for muon colliders and neutrino factories must be validated before a facility based upon these could be proposed. Such validation is usually made in dedicated test facilities, which are specially designed to address the major issues. These test facilities are expensive to build and operate, and are difficult to justify and fund, especially given that they are often useful only for technology development rather than for physics. An alternative approach, proposed by MASS, consists of a series of facilities built in stages, where each stage offers:

- Unique physics capabilities such that the facility obtains support and can be funded.
- In parallel with the physics program, integration of an R&D platform using each stage as a source of particles to develop, test with beam and validate a new technology that will be necessary for the following stages.
- A system based on the new technology, which when validated to work could be used to improve the performance of an existing facility, even if it is not necessary for the present stage.
- Operation of the new technology in a realistic environment, which is extremely useful not only to validate the new technology itself, but also to acquire operational experience before using it in a subsequent stage.
- Construction of each stage as an add-on to the previous stages, extensively reusing the equipment and systems already installed, such that the additional budget of each stage remains affordable.

The plan consists of a series of facilities with increasing complexity, each with performance characteristics providing unique physics reach:

- nuSTORM: As described in this article, the facility provides both a powerful neutrino physics program and the infrastructure to test new technologies.
- NuMAX: an initial long-baseline Neutrino Factory, optimized for a detector at Stanford Underground Research Facility (SURF) (142), affording a precise and well-characterized neutrino source that exceeds the capabilities of conventional superbeam technology.
- NuMAX+: a full-intensity Neutrino Factory, upgraded from NuMAX, as the ultimate source to enable precision CP-violation measurements in the neutrino sector.
- Higgs Factory: a collider whose baseline configurations are capable of providing between 3500 (during startup operations) and 13,500 Higgs events per year (10^7 sec) with exquisite energy resolution.
- Multi-TeV $\mu^+\mu^-$ Collider: if warranted by LHC results, a multi-TeV muon collider likely offers the best performance and least cost for any lepton collider operating in the multi-TeV regime.

Each stage in this scheme can serve as a technology validation test-bed for the following stage. The key example is nuSTORM, that does not require any state-of-the-art R&D, and at the same time can serve as a facility for a 6D cooling demonstration, as described in Section 6.4.

8. Outlook

In this article we have reviewed the potential of the nuSTORM facility. It can simultaneously produce flavor-pure neutrino beams from the decays of both pions and muons and can, as well, provide an intense low energy muon beam at the same time from the same proton power. Thus, the nuSTORM facility can simultaneously provide: 1. SBL oscillation measurements leading to a definitive solution to the sterile neutrino question and, should they exist, allow for the most comprehensive program to study their properties proposed to date, 2. Make world-leading measurements of neutrino interactions that could be crucial to the success of planned LBL neutrino programs and 3. Host an excellent R&D platform for 6D muon ionization cooling channel bench and beam tests and, as such, act as a stepping stone towards future high-energy high-intensity muon accelerator facilities.

The opportunities afforded by such a facility are great, but at the present time it lacks the formal support required to become a reality. Because nuSTORM has a relatively short construction time and leads into a sustained R&D program, it has the potential for enhancing the long-term prospects for neutrino physics, as well as sustaining a nascent muon collider community. The growth and development of neutrino physics and energy-frontier science will require pursuing new ideas and making them viable. The anticipated long time scales of the next generation of facilities will eventually limit the growth of the field, if they completely preclude embracing new ideas and innovation.

ACKNOWLEDGMENTS

The authors want to thank our colleagues in the Muon Collider and Neutrino Factor communities in general and, in particular, our collaborators on nuSTORM, MICE and in MAP. We want to offer special thanks to David Neuffer, who started down this path over 30 years ago and to Ao Liu who has worked so tirelessly on developing the nuSTORM facility. This work supported by the Fermi Research Alliance, LLC under Contract No. DE-AC02-07CH11359 with the United States Department of Energy, the Muon Accelerator Program within the United States Department of Energy and the Science and Technology Facilities Council of the United Kingdom.

LITERATURE CITED

1. Adey D, et al. nuSTORM - Neutrinos from STORed Muons: Proposal to the Fermilab PAC arXiv:1308.6822 [physics.acc-ph] (2013)
2. Bross A. 2013. In *Proceedings of the North American Part. Acc. Conf.*, no. TUOBD4
3. Bross A. 2013. In *Proceedings, of the 2013 Euro. Phys. Soc. Conf. on HEP*, vol. EPS-HEP2013
4. Geer S. *Phys.Rev.* D57:6989 (1998)
5. Giesch M, Kuiper B, van der Meer S. *Nucl. Instrum. Methods* 20:58 (1963)
6. Choubey S, et al. Interim Design Report for the International Design Study for a Neutrino Factory arXiv:1112.2853 [hep-ex] (2011)
7. Abe K, et al. Measurement of the Inclusive Electron Neutrino Charged Current Cross Section on Carbon with the T2K Near Detector arXiv:1407.7389 [hep-ex] (2014)
8. Adams C, et al. Scientific Opportunities with the Long-Baseline Neutrino Experiment (2013), FERMILAB-CONF-13-300
9. Agostino L. *J.Phys.Conf.Ser.* 566:012002 (2014)
10. Mohapatra R. *Phys.Rev.Lett.* 56:561 (1986)
11. Mohapatra R. *Phys.Rev.* D34:3457 (1986)

12. Kusenko A, Takahashi F, Yanagida TT. *Phys.Lett.* B693:144 (2010)
13. Abazajian K, et al. Light Sterile Neutrinos: A White Paper arXiv:1204.5379 [hep-ph] (2012)
14. Aguilar A, et al. *Phys. Rev.* D64:112007 (2001)
15. Aguilar-Arevalo A, et al. *Phys.Rev.Lett.* 110:161801 (2013)
16. Anselmann P, et al. *Phys.Lett.* B342:440 (1995)
17. Hampel W, et al. *Phys.Lett.* B420:114 (1998)
18. Abdurashitov D, et al. *Phys.Rev.Lett.* 77:4708 (1996)
19. Abdurashitov J, et al. *Phys.Rev.* C59:2246 (1999)
20. Abdurashitov J, et al. *Phys.Rev.* C73:045805 (2006)
21. Mention G, et al. *Phys.Rev.* D83:073006 (2011)
22. Mueller T, et al. *Phys.Rev.* C83:054615 (2011)
23. Huber P. *Phys.Rev.* C84:024617 (2011)
24. Huber P, Bross A, Palmer M. The Case for Muon-based Neutrino Beams arXiv:1411.0629 [hep-ex] (2014)
25. Borodovsky L, et al. *Phys.Rev.Lett.* 68:274 (1992)
26. Armbruster B, et al. *Phys. Rev.* D65:112001 (2002)
27. Astier P, et al. *Nucl. Phys.* B611:3 (2001)
28. Antonello M, et al. Experimental search for the LSND anomaly with the ICARUS LAr TPC detector in the CNGS beam arXiv:1209.0122 [hep-ex] (2012)
29. Ashie Y, et al. *Phys. Rev.* D71:112005 (2005)
30. Cleveland B, et al. *Astrophys. J.* 496:505 (1998)
31. Kaether F, et al. *Phys.Lett.* B685:47 (2010)
32. Abdurashitov J, et al. *Phys. Rev.* C80:015807 (2009)
33. Hosaka J, et al. *Phys. Rev.* D73:112001 (2006)
34. Aharmim B, et al. *Phys. Rev.* C75:045502 (2007)
35. Aharmim B, et al. *Phys. Rev.* C72:055502 (2005)
36. Aharmim B, et al. *Phys. Rev. Lett.* 101:111301 (2008)
37. Aharmim B, et al. Combined Analysis of all Three Phases of Solar Neutrino Data from the Sudbury Neutrino Observatory arXiv:1109.0763 [nucl-ex] (2011)
38. Bellini G, et al. *Phys.Rev.Lett.* 107:141302 (2011)
39. Bellini G, et al. *Phys.Rev.* D82:033006 (2010)
40. Aguilar-Arevalo AA, et al. *Phys.Rev.Lett.* 103:061802 (2009)
41. Cheng G, et al. *Phys.Rev.* D86:052009 (2012)
42. Adamson P, et al. *Phys.Rev.* D81:052004 (2010)
43. Adamson P, et al. *Phys.Rev.Lett.* 107:011802 (2011)
44. Declais Y, et al. *Nucl.Phys.* B434:503 (1995)
45. Declais Y, et al. *Phys.Lett.* B338:383 (1994)
46. Kuvshinnikov A, et al. *JETP Lett.* 54:253 (1991)
47. Vidyakin G, et al. *Sov.Phys.JETP* 66:243 (1987)
48. Kwon H, et al. *Phys.Rev.* D24:1097 (1981)
49. Zacek G, et al. *Phys. Rev.* D34:2621 (1986)
50. Apollonio M, et al. *Eur. Phys. J.* C27:331 (2003)
51. Boehm F, et al. *Phys.Rev.* D64:112001 (2001)
52. Abe Y, et al. *Phys.Rev.* D86:052008 (2012)
53. Ahn J, et al. *Phys.Rev.Lett.* 108:191802 (2012)
54. Gando A, et al. *Phys.Rev.* D83:052002 (2011)
55. Dydak F, et al. *Phys.Lett.* B134:281 (1984)
56. Reichenbacher J. Final KARMEN results (2005), Report:FZKA-7093
57. Auerbach L, et al. *Phys.Rev.* C64:065501 (2001)
58. Kopp J, Maltoni M, Schwetz T. *Phys.Rev.Lett.* 107:091801 (2011)
59. Giunti C, Laveder M. *Phys.Lett.* B706:200 (2011)

60. Karagiorgi G. Confronting Recent Neutrino Oscillation Data with Sterile Neutrinos arXiv:1110.3735 [hep-ph] (2011)
61. Giunti C, Laveder M. *Phys.Rev.* D84:093006 (2011)
62. Giunti C, Laveder M. *Phys.Rev.* D84:073008 (2011)
63. Giunti C, et al. *Phys.Rev.* D86:113014 (2012)
64. Archidiacono M, et al. Sterile Neutrinos: Cosmology vs Short-Baseline Experiments arXiv:1302.6720 [astro-ph.CO] (2013)
65. Kopp J, Machado P, Maltoni M, Schwetz T. Sterile Neutrino Oscillations: The Global Picture arXiv:1303.3011 [hep-ph] (2013)
66. An F, et al. *Phys.Rev.Lett.* 113:141802 (2014)
67. Sousa A. First MINOS+ Data (2014), Neutrino 2014, Boston MA. USA
68. Abe K, et al. Search for short baseline ν_e disappearance with the T2K near detector arXiv:1410.8811 [hep-ex] (2014)
69. Ade P, et al. *Astron.Astrophys.* 571:A16 (2014)
70. Hinshaw G, et al. Nine-Year Wilkinson Microwave Anisotropy Probe (WMAP) Observations: Cosmological Parameter Results arXiv:1212.5226 [astro-ph.CO] (2012)
71. Das S, et al. The Atacama Cosmology Telescope: Temperature and Gravitational Lensing Power Spectrum Measurements from Three Seasons of Data arXiv:1301.1037 [astro-ph.CO] (2013)
72. Reichardt C, et al. *Astrophys.J.* 755:70 (2012)
73. Story K, et al. A Measurement of the Cosmic Microwave Background Damping Tail from the 2500-square-degree SPT-SZ survey arXiv:1210.7231 [astro-ph.CO] (2012)
74. Percival WJ, et al. *Mon.Not.Roy.Astron.Soc.* 401:2148 (2010)
75. Padmanabhan N, et al. A 2Oscillations - I : Methods and Application to the Sloan Digital Sky Survey arXiv:1202.0090 [astro-ph.CO] (2012)
76. Blake C, et al. *Mon.Not.Roy.Astron.Soc.* 418:1707 (2011)
77. Anderson L, et al. *Mon.Not.Roy.Astron.Soc.* 427:3435 (2013)
78. Hannestad S, Hansen RS, Tram T. *Phys.Rev.Lett.* 112:031802 (2014)
79. Dasgupta B, Kopp J. *Phys.Rev.Lett.* 112:031803 (2014)
80. Mirizzi A, Mangano G, Pisanti O, Saviano N. Collisional production of sterile neutrinos via secret interactions and cosmological implications arXiv:1410.1385 [hep-ph] (2014)
81. Huber P, Mezzetto M, Schwetz T. *JHEP* 0803:021 (2008)
82. Neuffer D. Design Considerations for a Muon Storage Ring (1980), Telmark Conference on Neutrino Mass, Barger and Cline eds., Telmark, Wisconsin
83. Neuffer D, Liu A. 2013. In *Proceedings of the 4th Int. Part. Acc. Conf.* , no. TUPFI055
84. Liu A, Bross A, Neuffer D, Lee SY. 2013. In *Proceedings of the N. American Part. Acc. Conf.*, no. TUPBA18
85. Liu A, Neuffer D, Bross A, Lee S. Design and simulation of the nustorm injection beam line To be submitted to PRSTAB
86. Lackowski T, et al. nuSTORM Project Definition Report arXiv:1309.1389 [physics.ins-det] (2013)
87. Anderson K, et al. The NuMI Facility Technical Design Report (1998)
88. Wildner E. 2014. In *Proceedings of the XVIth International Workshop on Neutrino Factories and Future Neutrino Facilities (to be published)*
89. Adey D, et al. Neutrinos from Stored Muons nuSTORM: Expression of Interest arXiv:1305.1419 [physics.acc-ph] (2013)
90. Liu A, Bross A, Neuffer D. 2014. In *Proceedings, 5th Int. Part. Acc. Conf*, no. TUPRI005
91. Yamanoi Y, et al. *IEEE Trans.Magnetics* 32:2147 (1996)
92. Roberts T. G4beamline - A "Swiss Army Knife" for Geant4, optimized for simulating beamline (2013), Version 2.12
93. Courant E, Snyder H. *Annals Phys.* 3:1 (1958)

94. Liu A, Bross A, Neuffer D. 2014. In *Proceedings, 5th Int. Part. Acc. Conf*, no. IPAC-2014-TUPRI006
95. Neuffer D. 2014. In *Proceedings of the XVIth International Workshop on Neutrino Factories and Future Neutrino Facilities (to be published)*
96. Lagrange J. 2014. In *Proceedings of the XVIth International Workshop on Neutrino Factories and Future Neutrino Facilities (to be published)*
97. Lagrange J, et al. 2014. In *Proceedings, 5th Int. Part. Acc. Conf*, no. IPAC-2014-TUPRO073
98. Appleby R, et al. 2014. In *Proceedings, 5th Int. Part. Acc. Conf*, no. IPAC-2014-TUPRI013
99. S∅by L. nuSTORM Beam instrumentation (2013), eDMS document number: 1284677, CERN
100. Guardincerri E. *J.Phys.Conf.Ser.* 404:012036 (2012)
101. Rubbia A. *J.Phys.Conf.Ser.* 408:012006 (2013)
102. Michael DG, et al. *Nucl. Instrum. Meth.* A596:190 (2008)
103. Ambrosio G, et al. Design study for a staged very large hadron collider (2001)
104. Vysotsky V, et al. *IEEE Trans.Appl.Supercond.* 20:402 (2010)
105. Foussart A, et al. *IEEE Trans.Appl.Supercond.* 22:42000505 (2012)
106. Wesche R, et al. Results of conductor testing in SULTAN: A review (2009)
107. Adey D. 2014. In *Proceedings of the XVIth International Workshop on Neutrino Factories and Future Neutrino Facilities (to be published)*
108. Mokhov N, Striganov S. MARS15 Overview (2007), FERMILAB-CONF-07-008
109. Andreopoulos C, et al. *Nucl. Instrum. Meth. A* 614:87 (2010)
110. Apostolakis J, Wright DH. *AIP Conf. Proc.* 896:1 (2007)
111. Bayes R, et al. *Phys.Rev.* D86:093015 (2012)
112. Hoecker A, et al. *PoS* ACAT:040 (2007)
113. Brun R, Rademakers F. *Nucl. Instrum. Meth.* A389:81 (1997)
114. Huber P, Lindner M, Winter W. *Comput. Phys. Commun.* 167:195 (2005)
115. Baller B, et al. *JINST* 9:T05005 (2014)
116. de Gouvêa A, Kelly KJ, Kobach A. CP-Invariance Violation at Short-Baseline Experiments in 3+1 Scenarios arXiv:1412.1479 [hep-ph] (2014)
117. Gallardo J, et al. *eConf* C960625:R4 (1996)
118. Ankenbrandt CM, et al. *Phys.Rev.ST Accel.Beams* 2:081001 (1999)
119. Alsharo'a MM, et al. *Phys. Rev. ST Accel. Beams* 6:081001 (2003)
120. Parkhomchuk V, Skrinsky A. *AIP Conf.Proc.* 352:7 (1996)
121. Neuffer D. *AIP Conf.Proc.* 156:201 (1987)
122. Geer S. *Annual Review of Nuclear and Particle Science* 59:347 (2009)
123. Budker G. 1970. In *Proceedings of 15th International Conference on High Energy Physics*. Kiev
124. Neuffer D. *Part.Accel.* 14:75 (1983)
125. Palmer R, et al. *Phys. Rev. ST Accel. Beams* 8:061003 (2005)
126. The Neutrino Factory and Muon Collider Collaboration (NFMCC) `http://www.cap.bnl.gov/mumu/`
127. Muon Accelerator Program (MAP) `http://map.fnal.gov/`
128. Palmer M. 2014. In *Proceedings of 5th Int. Part. Acc. Conf.*, no. TUPME012. Dresden, Germany
129. Palmer M. 2013. In *Proceedings of COOL2013*, no. MOAM2HA02. Murren, Switzerland
130. Torun Y, et al. 2010. In *Proceedings of IPAC'10*, no. WEPE065. Kyoto, Japan
131. Delahaye JP, et al. Enabling Intensity and Energy Frontier Science with a Muon Accelerator Facility in the U.S.: A White Paper Submitted to the 2013 U.S. Community Summer Study of the Division of Particles and Fields of the American Physical Society arXiv:1308.0494 [physics.acc-ph] (2013)
132. Delahaye JP, et al. 2014. In *Proceedings, 5th Int. Part. Acc. Conf*, no. IPAC-2014-WEZA02
133. Bogomilov M, et al. *Phys.Rev.ST Accel.Beams* 17:121002 (2014)

134. Stratakis D, Fernow R, Berg J, Palmer R. *Phys. Rev. ST Accel. Beams* 16:091001 (2013)
135. Stratakis D, Neuffer D. 2014. In *Proceedings of the 5th Int. Part. Acc. Conf.*, no. TUPME021. Dresden, Germany
136. Derbenev Y, Johnson R. *Phys. Rev. ST Accel. Beams* 8:041002 (2005)
137. Yonehara K. 2014. In *Proceedings of 5th Int. Part. Acc. Conf.*, no. TUPME014. Dresden, Germany
138. Yonehara K. 2014. In *Proceedings of 5th Int. Part. Acc. Conf.*, no. TUPME015. Dresden, Germany
139. Hanlet P, et al. 2006. In *Proceedings of European Particle Accelerator Conference*, no. TUPCH147. Edinburgh
140. MICE collaboration `http://mice.iit.edu/`
141. Kaplan D, Snopok P, Dobbs A. 2014. In *Proceedings of 5th Int. Part. Acc. Conf.*, no. THPRI030. Dresden, Germany
142. Heise J. *AIP Conf.Proc.* 1604:331 (2014)